Journal of Applied Fluid Mechanics, Vol. 17, No. 5, pp. 1129-1142, 2024.
Available online at www.jafmonline.net, ISSN 1735-3572, EISSN 1735-3645.
https://doi.org/10.47176/jafm.17.05.2240

Numerical Study on Drag Reduction of Superhydrophobic Surfaces with Conical Microstructures in Laminar Flow

Y. Xu, C. Ruan† and Z. Zhang

School of Mathematics and Statistics, Henan University of Science and Technology, Luoyang, 471023, China

†Corresponding Author Email: ruanchunlei@haust.edu.cn

ABSTRACT

Superhydrophobic surfaces have garnered attention for their ability to decrease fluid resistance, which can significantly reduce energy consumption. This study aims to accurately capture critical flow phenomena in a microchannel and explore the internal drag-reduction mechanism of the flow field. To achieve this, the three-dimensional (3D) superhydrophobic surface flow field with conical microstructure is numerically simulated using the gas–liquid two-phase flow theory and Volume of Fluid (VOF) model, combined with a Semi-implicit method for the pressure-linked equation (SIMPLE) algorithm. The surface drag-reduction effect of the conical microstructure is investigated and compared it to that of the V-longitudinal groove and V-transverse groove surfaces. Additionally, the changes in the drag-reduction effect during the wear of the conical microstructure were explored. The numerical results reveal that the drag-reduction effect improves with a larger period spacing of the conical microstructure, the drag reduction rate can reach 25.23%. As the height of the conical microstructure increases, the aspect ratio (ratio of width to height) decreases, and the dimensionless pressure drop ratio and the drag-reduction ratio increase. When the aspect ratio approaches 1, the drag reduction rate can reach over 28%. indicating a more effective drag-reduction. The microstructure is most effective in reducing drag at the beginning of the wear period but becomes less effective as the wear level increases, when the high wear reaches 10, the drag reduction rate decreases to 3%. Compared to the V-shaped longitudinal groove and V-shaped transverse grooves, the conical microstructure is the most effective in reducing drag.

Article History

Received August 20, 2023
Revised December 25, 2023
Accepted December 31, 2023
Available online February 24, 2024

Keywords:

Superhydrophobic surface
Drag reduction
Numerical simulation
Conical microstructure
3D flow field

1. INTRODUCTION

With the rapid development of micro- and nanotechnology, superhydrophobic surfaces have garnered significant attention and have been employed (Monfared et al., 2019; Kibar, 2022). Researchers have fabricated microstructures, such as microgrooves and microcolumns, on smooth solid surfaces through hot pressing, lithography, and other methods. By exploring the drag-reduction mechanism of bionic surfaces, they have found that the sufficiently small size between adjacent microstructures results in a Cassie-Baxter state (Cassie, 1944), whereby the liquid flows over the surface without completely wetting the solid surface. This reduces the viscous resistance, generating a significant effective slip length (Davies et al., 2006).

To date, there have been numerous analytical, numerical, and experimental studies conducted on drag reduction in microchannels using superhydrophobic surfaces. In terms of experimental measurements, Ou et al. (2004) surveyed the pressure drop on a superhydrophobic surface using a rectangular experimental flow cell and found the pressure drop to be as high as 40%. They also observed the presence of a shear-free gas–liquid interface using a confocal surface metrology system, which they considered the key factor in the drag reduction in laminar flow. Ou and Rothstein (2005) measured the surface slip velocity using micron-resolution particle image velocimetry (PIV) and found that the drag-reduction mechanism mainly lies in the slip of the shear-free gas–liquid interface. They found that the maximum slip velocity was 60% higher than the average. Liu et al. (2019) developed a superhydrophobic surface with sharkskin patterns and found that the surface could achieve 21.7% drag-reduction underwater using a rotational viscometer.

In addition to experimental studies, numerical flow investigations in channels containing superhydrophobic

surfaces have been extensively conducted. Rastegari and Akhavan (2019) employed the lattice Boltzmann method in their study and found that the morphology and size of the superhydrophobic surface microstructure can impact its drag-reduction performance. Hosseini et al. (2019) used molecular dynamics research methods to analyze changes in the wetting state of superhydrophobic surfaces with different geometric morphologies. They discovered that increasing the adjacent spacing of microcolumns results in a smaller contact angle, therefore microcolumn spacing should be controlled during preparation. Watanabe et al. (2017) performed direct numerical simulation (DNS) to investigate flow in superhydrophobic microchannels under turbulent conditions. They observed that the average velocity rate increases by approximately 15% when using down-flow microridges, and the resistance reduction decreases with increasing slip rate as the angle of the microridges increases. Song et al. (2012) conducted a two-dimensional (2D) numerical simulation of a superhydrophobic surface and found that the drag-reduction rate increased with an increasing gas–liquid area ratio. They also reported that the drag reduction was almost independent of cavity height, and rectangular cavities showed better drag reduction than V-shaped and U-shaped cavities. Li et al. (2016) performed a 2D numerical simulation of superhydrophobic microchannels with rectangular cavities and found that the pressure drop increased with the gas–liquid area ratio. Cui et al. (2017) explored the performance of transverse microgrooves in drag reduction in three dimensions using the Volume of Fluid (VOF) model. Their results showed that the surface with transverse microgrooves has an effect of increasing resistance; however, the transverse grooves demonstrated drag reduction with the increase in microgroove spacing. Xu et al. (2021) studied a bionic superhydrophobic surface with V-shaped grooves and detected that V-shaped grooves had the highest drag reduction compared to U-shaped and rectangular longitudinal grooves. Manda and Mazumdar (2023) used CFD to numerically study the heat transfer and flow characteristics in microchannels with different cross-sectional shapes. The study showed that the flow performance of microchannels with triangular cross-sections was better than that of microchannels with other shapes.

In the area of material preparation, researchers have used various techniques to fabricate superhydrophobic materials with diverse morphologies and exceptional drag-reduction effects (Monfared et al., 2019; Zhang et al., 2022). However, when preparing superhydrophobic surfaces,researchers often enhance superhydrophobicity by increasing the gas–liquid area ratio, which usually results in fragility and susceptibility to wear. In recent years, Chen et al. (2015) employed a layer-by-layer self-assembly method to etch a relatively stable superhydrophobic surface with a regular conical array to address the issue of wear resistance. Wang et al. (2020a) fabricated a superhydrophobic surface consisting of inverted conical microstructures by lithography, which can withstand ultrahigh-pressure loading. Wang et al. (2020b) prepared three different sizes of superhydrophobic surfaces with conical microstructures, and ship navigation experiments showed that superhydrophobic surfaces exhibited significant drag-reduction effects compared to traditional smooth walls.

Following previous investigations, the morphology and structural parameters of the microstructure significantly impact the drag reduction of superhydrophobic surfaces, and exploring how to improve the structural parameters to enhance the drag-reduction effect requires an in-depth study. With the advancement of microfabrication technology, hydrophobic materials with good drag-reduction effects and high stability have been prepared, such as references (Wang et al., 2020a) and (Wang et al., 2020b), whose microstructures are three-dimensional (3D) conical microstructures. Previous studies on resistance reduction in simplified 2D microstructures have been relatively comprehensive, and 3D simulations have been limited to longitudinal and transverse grooves, while the drag-reduction effect of 3D conical microstructures has rarely been reported. The specificity of the conical shape also presents new challenges for simulation. Additionally, the wear resistance of microstructures is currently receiving considerable attention (Milionis et al., 2016; Zhang et al., 2017), but little work has systematically evaluated the drag reduction of 3D conical microstructures in practical wear through numerical simulations. Therefore, there is a need to improve research on the drag reduction of conical microstructures after wear.

We aimed to investigate the drag-reduction mechanism of superhydrophobic surfaces with conical microstructures in laminar flow. Therefore, this study uses numerical simulations to analyze the influence of structural parameters on the drag-reduction effect of such surfaces with conical microstructures. The study focuses on practical manufacturing engineering and applications. The overall content is organized as follows: First, the drag-reduction performance of superhydrophobic surfaces with conical microstructures of three different sizes is studied and analyzed in detail, based on experimental materials reported in reference (Wang et al., 2020b). Second, the drag-reduction performance investigation during the wear process of the conical microstructure is presented. Third, the drag-reduction effects of superhydrophobic surfaces with conical microstructures are compared to those of V-shaped longitudinal and V-shaped transverse grooves. Finally, useful conclusions are drawn. The design and experimental measurement of superhydrophobic microchannels are extremely expensive. Numerical study reduces the costs. In this work, a parametric numerical study is used to explore the drag reduction of superhydrophobic surfaces with conical microstructures. The purpose of this work is that to obtain some useful data and provide some useful suggestions to the designers and experimenters who are interested in the superhydrophobic surfaces.

2. MODELS AND ALGORITHMS

2.1 Physical Models

Consider the 3D images depicting microstructures of

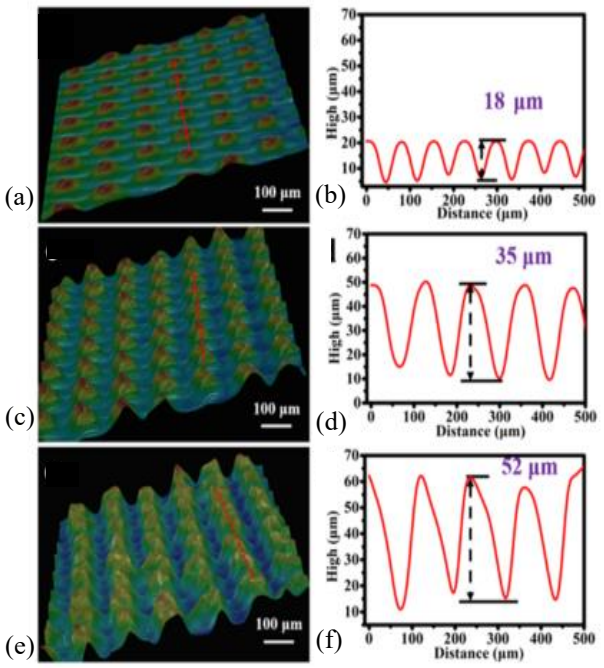

Fig. 1 3D micropatterned images (Wang et al., 2020b). (a)Samples prepared under 65℃hot-pressing conditions (H-65), (b)Width and height of micropattern H-65, (c)Samples prepared under 95℃hot-pressing conditions (H-95), (d)Width and height of micropattern H-95, (e)Samples prepared under 125℃hot-pressing conditions (H-125), (f)Width and height of micropattern H-125

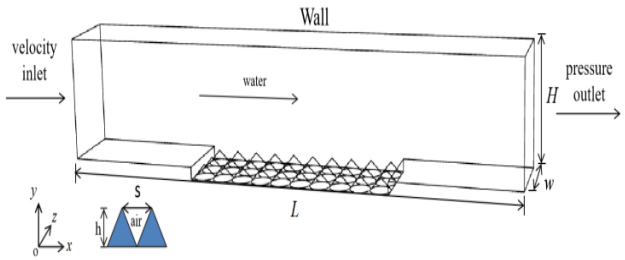

Fig. 2 Microchannel with conical microstructures

three distinct sizes, prepared as per reference (Wang et al., 2020b) and presented in Fig.1. The microstructures were physically modeled in this investigation and were characterized as 3D conical shapes, as demonstrated in Fig.2. In the physical model illustrated in Fig.2, the upper wall of the microchannel was smooth while the bottom surface featured rough conical microstructures. The cavities between adjacent microstructures were air-filled, and the water flow in the channels was assumed to be steady, incompressible, and laminar.

Here, the microchannel length, $L=2870\mu m$, width, $W=381\mu m$, and height, $H=500\mu m$. The microstructure height is denoted by h. In this model, s denotes a period and width of the conical microstructure. To minimize the effects of the inlet and outlet section and obtain convergence solutions, a smooth and no slip surface is taken at the inlet and outlet sections of the computational domain.

In actual experimental preparation, the maximum bottom diameter of the conical microstructure reaches $130\mu m$. In order to maintain consistency with the microstructure size prepared in the experiment, we comprehensively selected the microchannel length and width mentioned above. In this case, the hydraulic diameter $D_h=695\mu m$. If the flow in the microchannel needs to be fully developed before reaching the microstructure, one can refer to the formula proposed by Galvis et al. (Galvis et al. 2012) for the developing length, which is

$$\frac{L_{\text{int}}}{D_h}=\frac{0.715}{0.115\,\text{Re}+1}+0.0825\,\text{Re}$$

where, L_{int} is the inlet length, D_h is the hydraulic diameter, Re is the Reynolds number. For the case of our study, the developing length is $39964\mu m$ and the total length of microchannel should be $81198\mu m$. Considering the computational complexity and the ability of the computer, we have taken the microchannel length $L=2870\mu m$.

2.2 Mathematical Models

As shown in Fig.2, water flowing over microchannel and air filling the adjacent conical, forming a typical gas–liquid two-phase flow. This study employed the VOF model to determine the fluid volume fraction in the control volume and the gas–liquid interface.

Under steady isothermal laminar flow in the channel, the governing equations are the Navier-Stokes equations (Anderson, 1995). The continuity equation is expressed as follows

$$\frac{\partial u}{\partial x}+\frac{\partial v}{\partial y}+\frac{\partial w}{\partial z}=0 \tag{1}$$

Neglecting the effect of gravity, the momentum equation can be expressed as follows:

$$\begin{aligned}
&\rho u\frac{\partial u}{\partial x}+\rho v\frac{\partial u}{\partial y}+\rho w\frac{\partial u}{\partial z}=-\frac{\partial p}{\partial x}+\mu\left(\frac{\partial^2 u}{\partial x^2}+\frac{\partial^2 u}{\partial y^2}+\frac{\partial^2 u}{\partial z^2}\right),\\
&\rho u\frac{\partial v}{\partial x}+\rho v\frac{\partial v}{\partial y}+\rho w\frac{\partial v}{\partial z}=-\frac{\partial p}{\partial y}+\mu\left(\frac{\partial^2 v}{\partial x^2}+\frac{\partial^2 v}{\partial y^2}+\frac{\partial^2 v}{\partial z^2}\right),\\
&\rho u\frac{\partial w}{\partial x}+\rho v\frac{\partial w}{\partial y}+\rho w\frac{\partial w}{\partial z}=-\frac{\partial p}{\partial z}+\mu\left(\frac{\partial^2 w}{\partial x^2}+\frac{\partial^2 w}{\partial y^2}+\frac{\partial^2 w}{\partial z^2}\right)
\end{aligned} \tag{2}$$

where u,v,w are the velocities in the x,y,z directions, respectively. p is the pressure, ρ is the density, and μ is the viscosity coefficient. The density and dynamic viscosity are closed by the following mixing theorem:

$$\begin{aligned}
\rho&=\alpha_w\rho_w+(1-\alpha_w)\rho_a\\
\mu&=\alpha_w\mu_w+(1-\alpha_w)\mu_a
\end{aligned} \tag{3}$$

where ρ_w, μ_w are the density and viscosity coefficients of water, respectively, ρ_a and μ_a are the

density and viscosity coefficients of air, and α_w is the volume fraction of water. When $\alpha_w = 1$, the control volume is filled with water, and when $\alpha_w = 0$, the control volume is filled with air, and when $0 < \alpha_w < 1$, the control volume has two phases (water and air). The VOF equation is expressed as follows (Anderson, 1995)

$$\frac{\partial \alpha_w}{\partial t} + u\frac{\partial \alpha_w}{\partial x} + v\frac{\partial \alpha_w}{\partial y} + w\frac{\partial \alpha_w}{\partial z} = 0 \tag{4}$$

The boundary conditions for the computational domain are set as follows: the inlet velocity is $u_{in} = 1m/s$; the outlet pressure is set to be constant; the front and back walls are set as symmetric boundaries to simulate an infinite flat plate, and the rest of the walls are defined as no-slip boundaries. The initial condition is set as follows: The microchannel is full of water, and the cavity full of air. The gas–liquid interface is assumed to be flat.

The second-order upwind scheme is used to discretize convection term and second-order central scheme is used to discretize diffusion term in the momentum equation. Subsequently, the control equation is solved using the Semi-Implicit Method for Pressure-Linked Equations (SIMPLE) algorithm (Tao, 2001) To capture the interface between the water and air, the VOF model is employed, and the convergence residual is specified as 10^{-8}.

2.3 Dimensionless Pressure Drop Ratio and Drag-Reduction Rate

The following drag-reduction parameters were introduced to evaluate the drag-reduction effect of the superhydrophobic surfaces.

The dimensionless pressure drop ratio is expressed as follows (Ou et al., 2004)

$$\Pi = \frac{\Delta P_S - \Delta P}{\Delta P_S} \tag{5}$$

where ΔP_S and ΔP denote the average pressure drops of stable segments for smooth and superhydrophobic microchannels, respectively. Unless otherwise specified, the average pressure drops at sections $x = 864\mu m$ and $x = 2007\mu m$ are taken as the pressure drop in the stable section.

For steady, incompressible, laminar flow in a microchannel, the Poiseuille number is expressed as (Li et al., 2016):

$$f\,\mathrm{Re} = \frac{2\Delta P D_h^{\,2}}{u_{in}\mu B} \tag{6}$$

Where B denotes the length of the stable section of the desired average pressure drop, D_H is the hydraulic diameter, typically four times the cross-sectional area divided by the perimeter of the channel section, and can be expressed as follows:

$$D_H = \frac{2WH}{W+H} \tag{7}$$

The rate of reduction in resistance can be defined by comparing the total drag experienced by a smooth surface with that of a superhydrophobic surface:

$$DR = \frac{F_S - F}{F_S} \tag{8}$$

where F_S and F denote the total drag of the smooth and superhydrophobic surfaces，respectively.

3. RESULTS AND DISCUSSION

3.1 Validation

To demonstrate the accuracy of the numerical calculation, a comparison is made between the numerical results and the theoretical solution in a smooth microchannel. Furthermore, a comparison is provided between the numerical results and the experimental measurements obtained from microchannels exhibiting a columnar microstructure.

3.1.1 Flow in Smooth Microchannel

For incompressible fluid flows within a smooth rectangular channel with a thickness H, width W, and length L, the theoretical pressure drop can be calculated according to (Blevins, 1984):

$$\Delta P_S = \frac{\rho u_{in}^{\,2} fL}{2D_H} \tag{9}$$

where f denotes the average friction factor, inversely proportional to the Reynolds number, and calculated as follows:

$$f = \frac{k}{\mathrm{Re}} \tag{10}$$

where Re is the Reynolds number, $\mathrm{Re} = \frac{\rho v D_H}{\eta}$, η is the kinematic viscosity; k is the friction coefficient, obtained by solving the Poiseuille equation in the cross section and is expressed as follows (Yang et al., 2018):

$$k = \frac{64}{\frac{2}{3} + \frac{11}{23}\frac{H}{W}\left(2 - \frac{H}{W}\right)} \tag{11}$$

Figure 3 presents a comparison between numerical results and theoretical values within a smooth microchannel. The theoretical results were obtained using Eq. (9). As shown in Fig. 3, the simulation results agree qualitatively with the theoretical solutions. Therefore, the validity of the algorithm for simulating flow in a smooth channel is confirmed.

3.1.2 Flow in Columnar Microstructure Channels

Ou et al. (2004) conducted experimental measurements of the pressure drop in microchannels with columnar microstructures under laminar flow. The physical model is presented in Fig. 4. To validate the

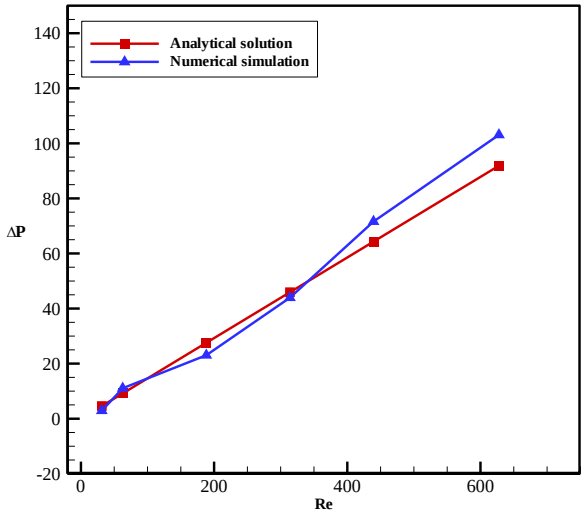

Fig. 3 Variation of the pressure drop with Reyolds number Re

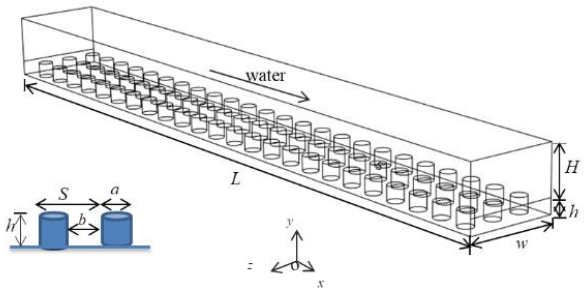

Fig. 4 Superhydrophobic microchannels with columnar microstructures

model and algorithm further, 3D numerical simulations were performed in channels with columnar microstructures.

Here, the channel length, $L=1800\mu m$, width, $W=180\mu m$, and height $h=a$. The distances between adjacent microstructures are taken as $15\mu m$, $30\mu m$, $60\mu m$, $150\mu m$. The shear-free area ratio defined as $\beta=(s-a)/s$. Figure 5 displays the grid for the cross-section, using a structured hexahedral mesh. Local refinement was applied to the region in which the flow field exhibits significant variation. The calculation employed approximately $80\times10^4\sim100\times10^4$ meshes.

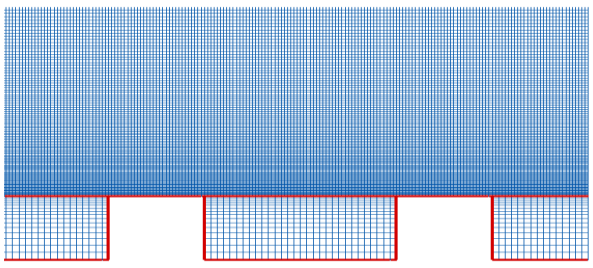

Fig. 5 Grid of microchannel with columnar microstructure in *xy* **cross-sectional**

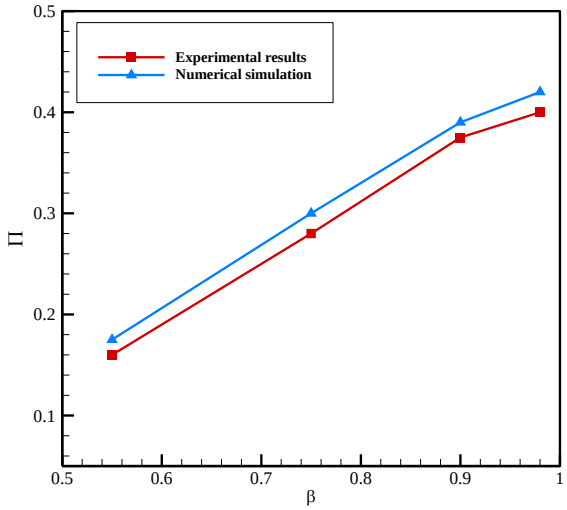

Fig. 6 Variation of dimensionless pressure drop ratio with shear-free area ratio

Figure 6 illustrates the comparison of the dimensionless pressure drop ratios obtained from numerical simulations with the experimental results (Ou et al., 2004). The simulation results demonstrate qualitative consistency with the experimental outcomes. For microchannels with superhydrophobicity and columnar microstructures, an increase in the gas–liquid area ratio leads to a rise in the dimensionless pressure drop ratio. However, the dimensionless pressure drop ratio obtained from the numerical simulations is higher than the experimental findings of Ou et al. (2004) . The average relative error is approximately 6.4%. This discrepancy may result from the idealized conditions used in the numerical simulations.

3.2 Analysis of the Drag-Reduction Effect of Conical Microstructures

Numerical simulations were used to discuss the drag-reduction performances of three sizes of conical microstructures, as reported in reference (Wang et al., 2020b). Table 1 presents the specific parameters of the microstructures. The Virgin film is the original mold that has not undergone any hot pressing treatment, i.e. a smooth surface.H-65, H-95, and H-125 correspond to superhydrophobic surfaces with conical microstructures prepared under hot pressing temperature conditions of 65 °C, 95 °C, and 125 °C, respectively. For the simulation, an unstructured polyhedral mesh was used, and local refinement was applied to areas near the conical surfaces. Figure 7 depicts the local mesh of the microchannel. To avoid the impact of grid number on the calculation results, we selected different numbers of grids for grid independence verification, as shown in Table 2. Solution obtained by grid number of 241×10^4 is selected as the reference. It was found that the change in resistance coefficient of superhydrophobic surfaces was less than 4%. Considering the calculation time and accuracy, the grid number is selected as 2412005 for the following simulation. In addition, the range of y plus values is 0<y<3.5.

Table 1 Microstructure parameters from Wang et al., (2020b)**)**

Name	Microstructure size(μm)	
	width *s*	height *h*
Virgin film	0	0
H-65	75	18
H-95	130	35
H-125	127	52

Table 2 Grid independence verification

Number of grids(10^4)	89	170	209	241	281
Drag coefficient deviation	3.96%	1.57%	1.32%	0	1.15%

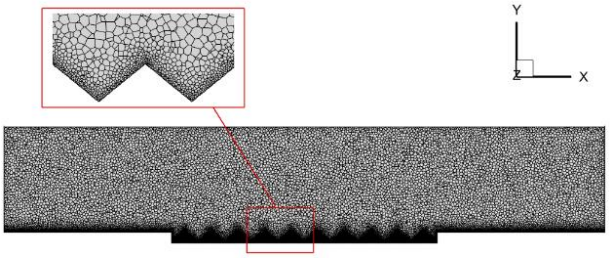

Fig. 7 Mesh within conical microstructure channels

3.2.1 Characterization in the Flow Field

Figure 8(a) illustrates the volume fraction contours for the cross-section. The surface tension creates a distinct gas–liquid interface between the water and air phases. Moreover, during the flow of water over the microchannel, the air is effectively trapped within the gaps. The gas–liquid interface exhibits a non-planar curvature, as shown in Fig. 8(b), this phenomenon is consistent with the findings of Ou et al. (2004) ,where the maximum deviation of curvature displacement is 9μm.

The velocity contour and velocity vector diagrams of the H-125 flow field in the cross-section are presented in Fig. 9. From Fig. 9(a), it is evident that the velocity stratification throughout the flow field is distinct, with lower velocity near the wall. The velocity fields near the upper and lower walls exhibit significant differences, and the velocity field near the lower wall becomes exceedingly complex. The presence of microstructures converts the original solid-liquid surface into a gas–liquid interface, resulting in a slip velocity that is clearly observed at the gas–liquid contact surface. In addition, we can also see some spurious currents at the gas-liquid interface, which may be due to the strong influence of the hydrostatic pressure in the channel on the gas pressure inside the cavity. The gas continuously diffuses and dissolves into the surrounding water, resulting in the instability of the flow field at the gas-liquid interface. It can be observed from Fig. 9(b) that the water flow is fully developed in the channel, and the gas forms a low-speed whirlpool inside the cavity. The upper part of the whirlpool

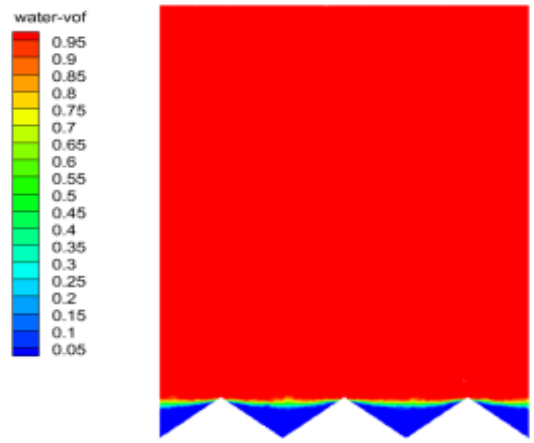

(a) Volume fraction contour

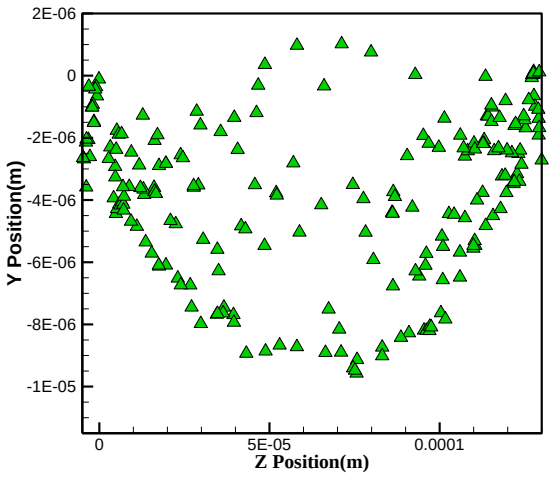

(b) Interfacial curvature displacement

Fig. 8 Phase field characteristics of *yz* **section**

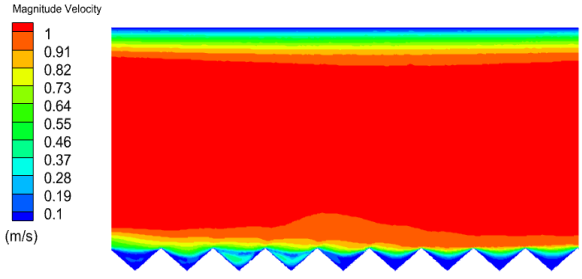

(a) Velocity Contour

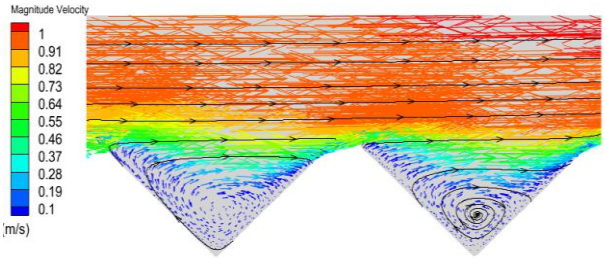

(b)Velocity vector

Fig. 9 Velocity field characteristics of *xy* **section**

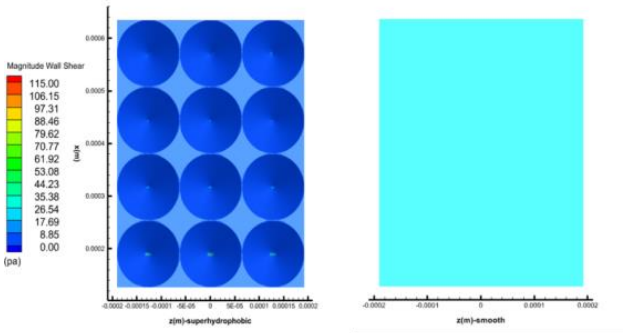

Fig. 10 Shear stress distribution contour for superhydrophobic and smooth surfaces

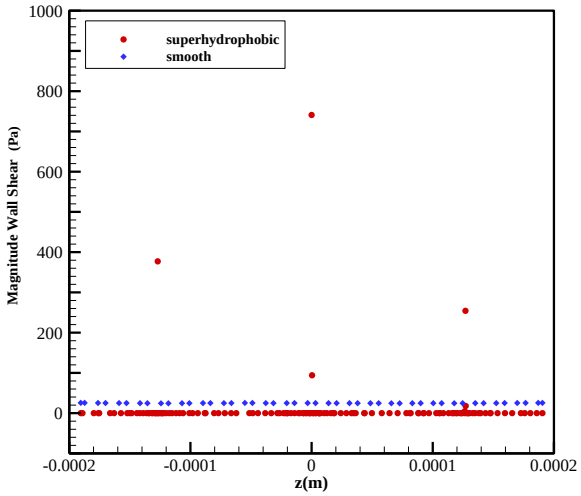

Fig. 11 Comparison of shear stress on superhydrophobic surface and smooth surfaces

is aligned with the water flow direction near the gas–liquid interface, generating a push effect and vortex cushion effect. These results are consistent with the simulation findings of Song et al. (2012) , who reported that the thrust and vortex cushion effects were responsible for achieving surface drag reduction.

Figure 10 displays the contour of the shear stress distribution for superhydrophobic and smooth walls. The presence of microstructures yields a significant difference in the shear stress generated on superhydrophobic surfaces compared to the uniform shear stress on smooth surfaces. Specifically, the shear stress on superhydrophobic surfaces can be categorized into two extremes: the shear stress is ultrahigh at the apex of the conical microstructure, and the shear stress is minimal, nearly zero, across the remainder of the microstructure, as illustrated in Fig. 11. Consequently, the overall average shear stress on the superhydrophobic surface is lower than that on the smooth surface, with the average shear stress on a smooth surface is 24.91Pa, and the average shear stress on a superhydrophobic surface is 6.53Pa.

3.2.2 Impact of Microstructure Size Parameters for Drag-Reduction Performance

Table 3 illustrates a comparison of the dimensionless pressure drop ratio, Poiseuille number, and drag-reduction rate for four distinct surfaces. The comparison demonstrates that a surface containing conical microstructures can effectively reduce drag. For three different sizes of conical microstructures, the dimensionless pressure drop can be reduced by up to 70%, and drag reduction can exceed 25%. The conical microstructure transforms the original solid-liquid contact surface into a gas–liquid contact face, thereby reducing viscous resistance. Moreover, as depicted in Table 3, H-125 exhibits the most significant drag-reduction effect, with the highest dimensionless pressure drop and drag-reduction rate. This finding agrees with the experimental results (Wang et al., 2020b).

Table 3 Comparison of the drag-reduction parameters of three microstructures and smooth surfaces

Name	Dimensionless pressure drop ratio	Poiseuille number	drag reduction rate (%)
Virgin film	0	68.95	0
H-65	0.35	45.09	23.47
H-95	0.64	24.51	24.41
H-125	0.72	19.23	25.23

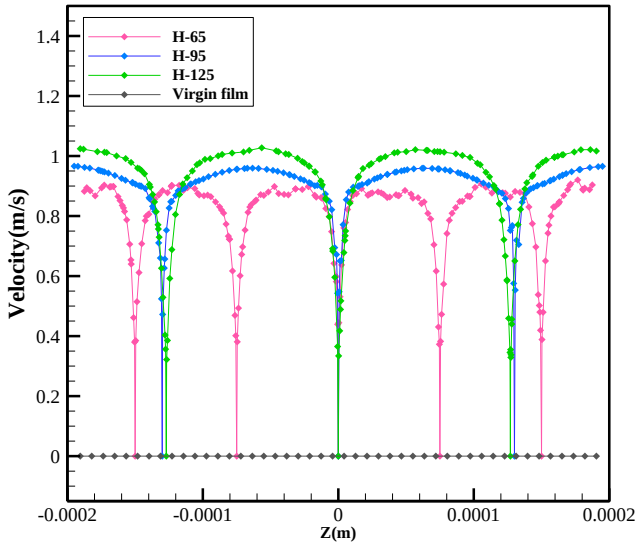

Fig. 12 Slip velocity along z-direction for three superhydrophobic and smooth surfaces

Figure 12 depicts the slip velocity along the z-axis for four distinct walls. The data illustrates that the no-slip wall has a slip velocity of 0, whereas the superhydrophobic surface generates a slip velocity. The superhydrophobic surface with conical microstructures exhibits a slip velocity of zero at the tip. Furthermore, the velocity is comparatively low in the vicinity of the tip and gradually increases until it reaches the maximum at the center of the adjacent microstructure. Given that the adjacent microstructure spacing of H-125 and H-95 is larger than that of H-65, the slip velocity of both surfaces is greater than that of H-65. The slip velocity of H-125 is slightly higher than that of H-95, consistent with the results presented in Table 2.

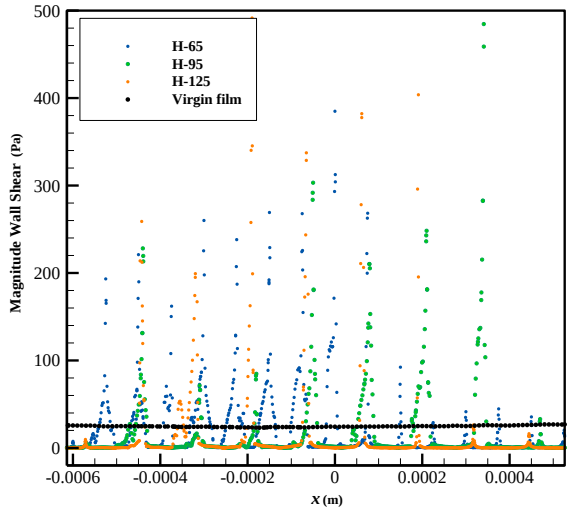

Fig. 13 Wall shear stress distribution along the *x*-direction

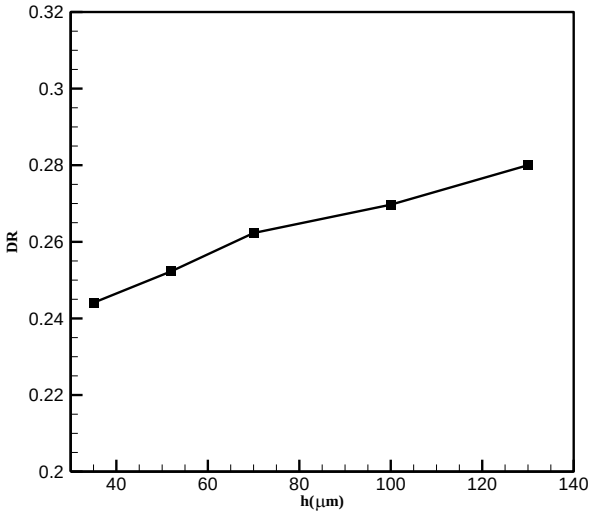

Fig. 14 Variation in drag reduction with microstructure height h

Figure 13 compares the wall shear stress along the x-direction for three different microstructures and smooth surfaces. The distribution of wall shear stress along the x-direction of the superhydrophobic surface varies significantly; however, it is more uniformly distributed than that of a smooth wall. H-125, H-95, and H-65 produce ultrahigh shear stresses near the tip, whereas they are nearly zero along the rest of the wall. Therefore, the overall shear stresses are lower than those on smooth surfaces. Additionally, as evident from Fig. 14, the average wall shear stress of H-125 is less than that of H-95 and H-65, consistent with the results obtained in Table 2.

Based on the processing technology (Wang et al., 2020b), the material is melted at high temperature, and the resulting sample completely replicates the structure of the template. When the pressure is increased beyond this point, the distance between adjacent microstructures

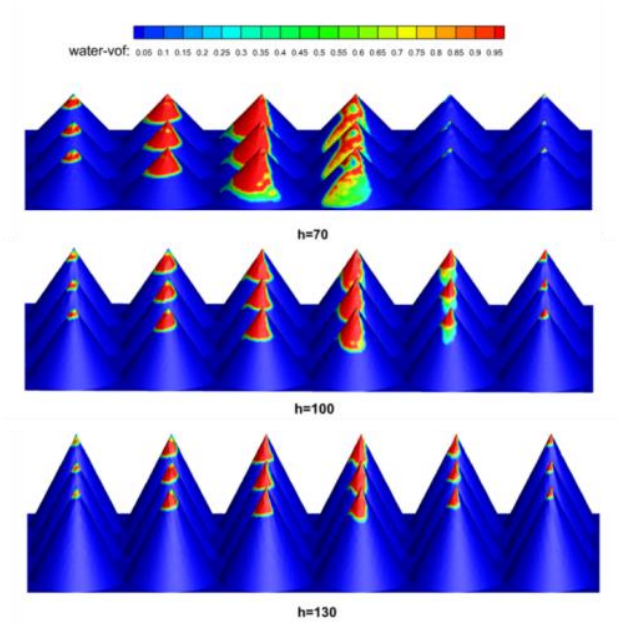

Fig. 15 Volume distribution of liquid infiltration with three different height microstructures

remains almost constant, while the height increases further. Consequently, this study assumes a constant microstructure width, while continuing to increase the height of the microstructure. Subsequently, three heights, $70\mu m$, $100\mu m$, and $130\mu m$ are investigated.

Figure 14 depicts the relationship between the height of the microstructure and the drag-reduction rate. Specifically, an increase in microstructure height is associated with a higher drag-reduction rate. This observation may be attributed to the unique morphology of the conical microstructure. At a constant microstructure width but increasing height, the aspect ratio (s/h) is reduced. When water flows over a superhydrophobic surface with conical microstructures, the contact surface between the liquid and the upper part of the cone is smaller, resulting in reduced viscous resistance. Figure 15 illustrates that for conical microstructures with higher aspect ratios, the infiltration area is larger when the liquid begins to infiltrate the upper part of the structure.

3.3 Analysis of Surface-Worn Effects with Conical Microstructures

Previous research has demonstrated that superhydrophobic surfaces are highly prone to wear (Tian et al., 2016), which alters the drag-reduction performance of these surfaces during or after wear. The tip of the cone is subjected to ultrahigh shear stress during use and is particularly susceptible to wear. This section primarily examines the variation in the drag-reduction effect of the conical microstructure during the wear process.

The practical applications considered in our work, the tip of the conical microstructure is gradually rounded to form a certain curvature during the initial stage of wear, it is noted here as parameter "*arc*." As the wear level increases, the "*arc*" gradually decreases, as illustrated in

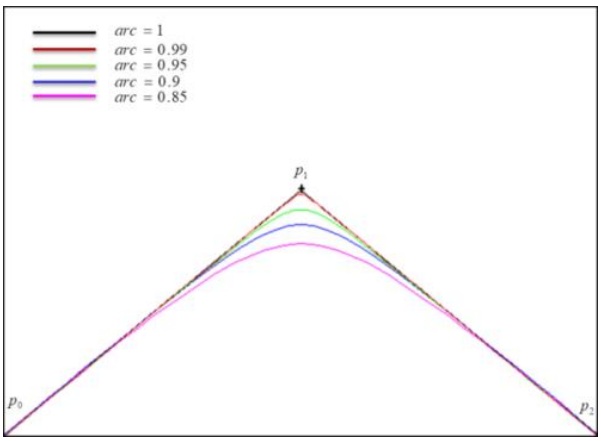

Fig. 16 Schematic diagram of parameter "*arc*"

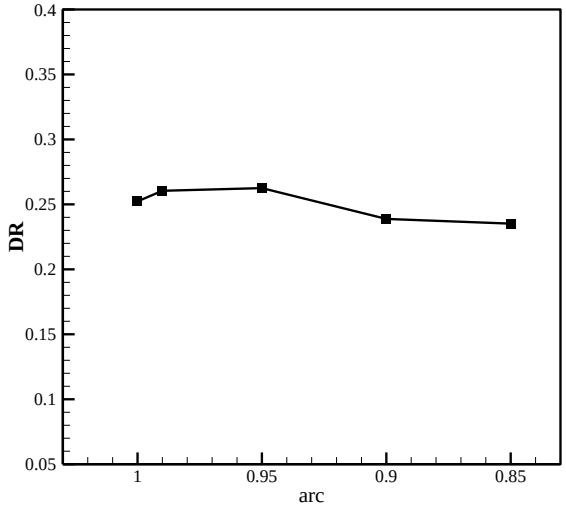

Fig. 17 Variation of drag-reduction rate of "*arc*"

Fig. 16. Therefore, a tip smoothing operation was used in the modeling.

A quadratic Bezier curve with shape parameters is employed to model a 2D curve and then rotated it to obtain a 3D physical model after wear. The quadratic Bezier is defined as follows: let $p_i(i=0,1,2)$ be a control point, then the quadratic Bezier curve with shape parameter is expressed as (Wang & Liu, 2007):

$$P(t)=\sum_{i=0}^{2} p_i b_i(t) \tag{12}$$

where $b_i(t)$ is a basis function:

$$\begin{cases} b_0(t)=1-\arcsin t+(arc-1)\sin^2 t \\ b_1(t)=-arc+\arcsin t+\arccos t \\ b_2(t)=arc-\arccos t+(1-arc)\sin^2 t \end{cases}, \quad 0\le t\le \frac{\pi}{2},$$

where "*arc*" is the shape parameter for determining the shape of the curve. As depicted in Fig. 16, the initial state when the tip is unworn is represented by $arc=1$. The

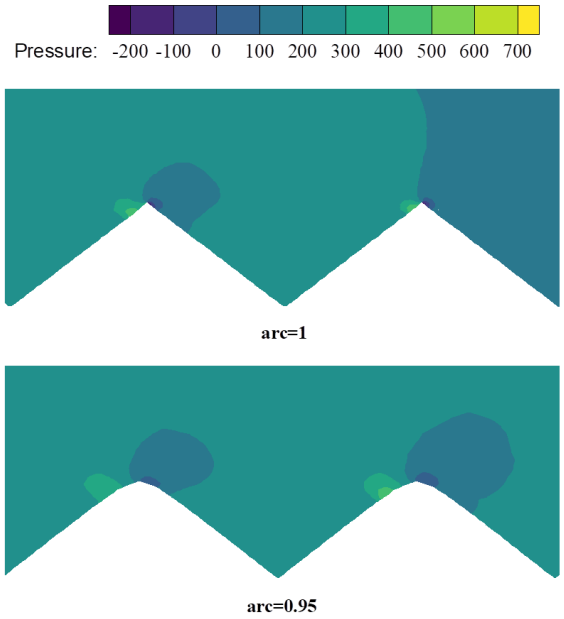

Fig. 18 Pressure contour of the worn microstructure tip along the flow direction (*x*-direction)

decrease in the arc parameter indicates a gradual change in the curvature of the microstructure tip as the degree of wear increases.

Figure 17 depicts the variation in surface drag-reduction rate with arc. As shown in the figure, the drag-reduction rate initially increases and then decreases with changes in the arc parameter. This phenomenon could be attributed to the gradual tip wear during the flow process, which subsequently decreases the pressure gradient ahead and behind the tip. This effect contributes to the drag reduction, which is slightly enhanced by low differential pressure resistance. However, an increase in wear degree reduces the differential pressure resistance while increasing the viscous resistance, leading to inferior performance. The pressure distribution near the top of the conical microstructure is presented in Fig. 18 for both pre-wear (*arc*=1) and post-wear (*arc*=0.95) conditions. The comparison between the two conditions reveals a significant reduction in pressure difference at the top of the tip after wear (*arc*=0.95) compared to that before wear (*arc*=1).

As the intensity of abrasion increases, or when nanoparticles interact with the water flow, the tip of the microstructure will flatten, and its height will decrease while its bottom remains microstructured. To investigate the changes in drag-reduction performance of microstructure during the wear process, a schematic diagram of four different heights during the wear process is given in Fig. 19. It is clear from the diagram that the conical microstructure gradually transforms into a round, table-shaped microstructure during the wear process.

Figure 20 illustrates the variation of the dimensionless parameters, namely the Poiseuille number and the drag-reduction rate, with the height of the microstructure. Decreasing the height of the round table microstructure causes a decrease in both the dimensionless

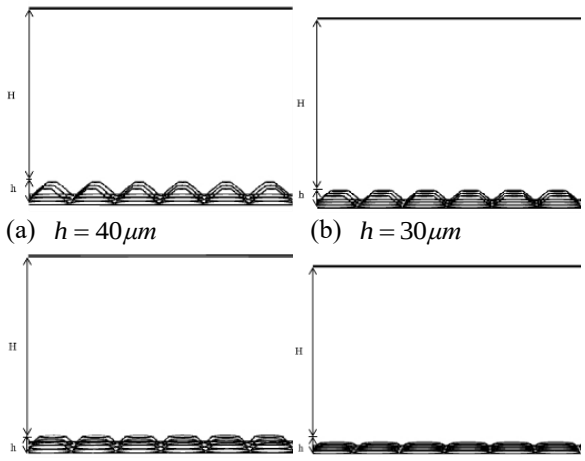

Fig. 19 Variation of the microstructure heightwith h wear process

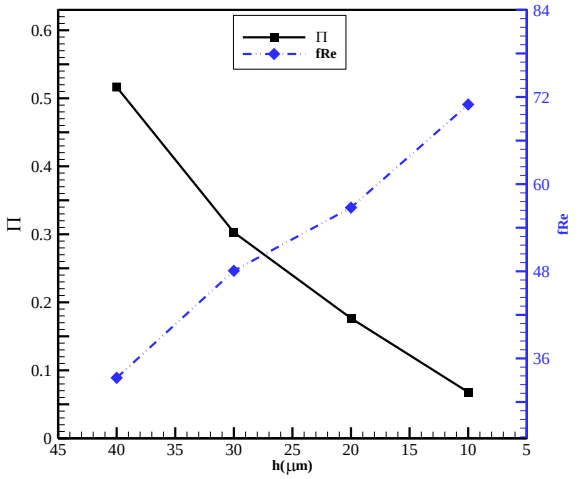

(a) Dimensionless pressure drop ratio and Poiseuille number

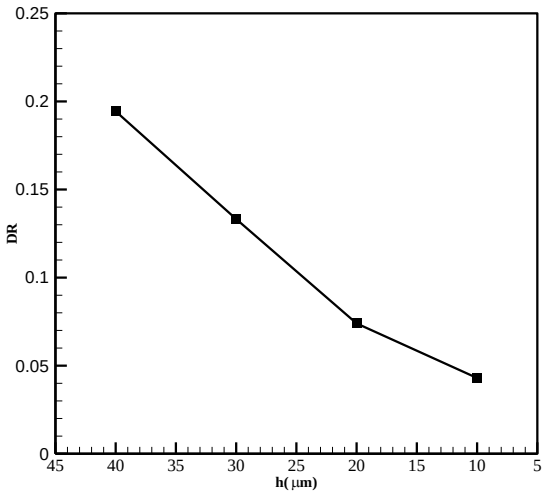

(b) drag-reduction rate

Fig. 20 Variation in drag-reduction parameters with microstructure height *h*

pressure drop ratio and the drag-reduction rate. In contrast, the Poiseuille number increases as the height of the round table microstructure decreases. As a result, the superhydrophobicity of the surface gradually deteriorates, ultimately falling below 5% during the wear process. This can be attributed to the following: first, the reduction in the height of the round stable microstructure led to a proportional increase in the solid-liquid contact surface and viscous resistance. Second, within microchannels of the same height, the relative height of the microchannel increases as the microstructure height decreases, thereby diminishing the impact of the superhydrophobic surface on the microchannel. Finally, as the height of the round table microstructure is reduced, the aspect ratio increases and the gap between adjacent microstructures decreases, which does not favor the formation of the vortex cushion effect between adjacent microstructures, and is thus not conducive to drag reduction.

In summary, the differential pressure resistance in the microchannel decreases when the conical microstructure becomes slightly worn, reducing drag. This phenomenon occurs when the tip of the microstructure is rounded at the beginning. However, as the wear of the tip continues to increase, viscous drag becomes dominant, resulting in poorer drag reduction. Therefore, during the preparation of the microstructure, it is advisable to round the tip appropriately while being mindful of a critical arc point. If the critical point is exceeded, i.e., the increase in viscous resistance is greater than the decrease in differential pressure resistance, it would not be conducive to reducing drag.

3.4 Comparison of the Drag-Reduction Effects of Different Shaped Microstructures

The study compared the drag-reduction effects of surfaces with varying microstructures. Specifically, the research examined the drag-reduction effects of superhydrophobic surfaces featuring V-shaped longitudinal grooves, V-shaped transverse grooves, and conical microstructures.

Figure 21 illustrates a superhydrophobic microchannel featuring a V-shaped groove that runs parallel to the flow direction, and another V-shaped groove perpendicular to the flow direction. To conduct a more thorough analysis of the drag-reduction effect of the tapered microstructure, the parameters of H-125 are taken for the conical microstructure, and the rounded table shape ($h=40\mu m$) after wear down is also considered. To simulate the V-transverse and V-longitudinal grooves, we set the period length between adjacent ribs of the groove to be identical to H-125 ($s=127\mu m$) and the groove height to be $h=52\mu m$.

Figure 22 presents a comparison of the drag-reduction rates of four different microstructures with distinct shapes. The figure demonstrates that the conical shape (H-125) exhibits the highest drag-reduction rate, while the reduction rate of the longitudinal groove, round table, and transverse groove decrease sequentially. This observation can be attributed to the following reasons: H-125 has the smallest solid-liquid contact surface owing to its shape, and the adjacent cones can better seal the gas between them, facilitating the formation of vortices in the gas phase. This vortex cushion effect results in a greater slip velocity.

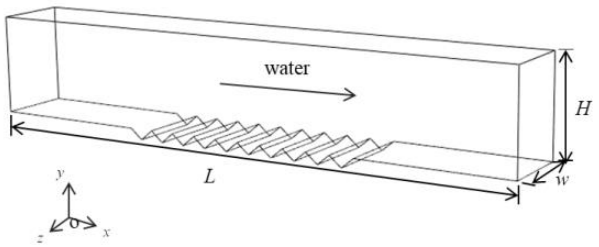

(a) V-shaped transverse (Perpendicular to the flow direction)

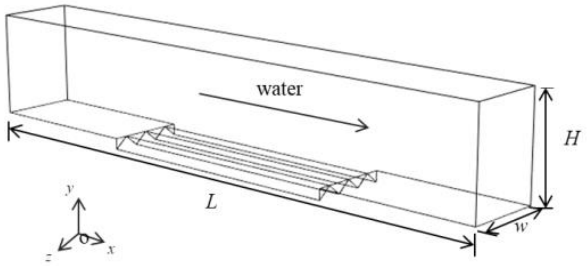

(b) V-shaped longitudinal groove (Parallel to the flow direction)

Fig. 21 V-shaped grooves

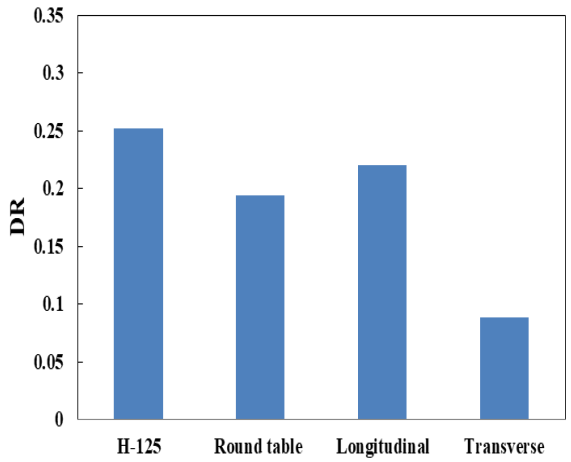

Fig. 22 Comparison of the resistance reduction rates of four different shaped microstructures

To analyze further the reasons for the difference in drag-reduction rates among the four shaped microstructures, this study compares and analyzes the average viscous resistance, wall shear stress, and differential pressure resistance of the superhydrophobic surfaces. As shown in Fig. 23, the red bars illustrate the viscous resistance, which is higher for the round table and longitudinal grooves and lower for the H-125 and transverse grooves. The conical, longitudinal, and transverse grooves transform the solid-liquid contact surface into sharp points or thin ribs. On the other hand, the round table has a flat top with a certain area of solid-liquid contact surface, resulting in greater viscous resistance. The longitudinal groove is parallel to the direction of flowing water, and the differential pressure resistance is minimal. However, it cannot form the vortex cushion effect, which is not conducive to the preservation of gas in the cavity, causing the gas loss to enlarge, leading to higher viscous resistance. The green bars

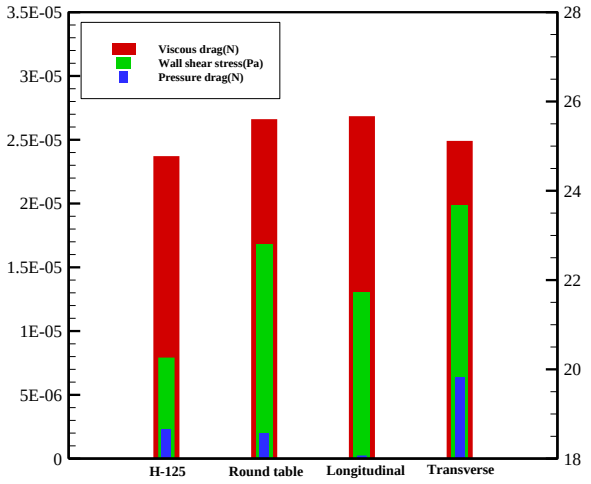

Fig. 23 Comparative analysis of viscous resistance, wall shear stress, and differential pressure resistance of different shaped microstructures

represent the average wall shear stress, which is higher for the round table and transverse grooves and lower for the H-125 and longitudinal grooves. The upper surface of the round table has zero slip velocity, resulting in a large velocity gradient at the front and end of the upper surface. Similarly, the transverse groove generates a large velocity gradient at each rib, so both the round table and the transverse groove have large shear stress. The blue bars represent differential pressure resistance, with the longitudinal groove having the lowest differential pressure resistance and the transverse groove the highest, with the H-125 and the round able microstructure in between. The longitudinal groove is in the same direction as the water flow, resulting in almost zero differential pressure resistance. The transverse groove is perpendicular to the direction of water flow and effectively traps gas in the V-shaped cavity to form a vortex cushion effect, resulting in less viscous resistance. However, the pressure difference is generated in front and behind each of its ribs, giving rise to a great differential pressure resistance, which corresponds to three times that of the H-125 and the round table. In addition, we found that the flow in microchannels is mainly affected by viscous resistance and pressure difference resistance, and reducing these two types of resistance becomes the key to reducing drag in microchannels. Currently, supercritical carbon dioxide (sCO2)(Manda et al., 2022) in microchannels has been explored as a potential alternative to traditional fluids such as water and air (Manda et al., 2023). sCO2 has low viscosity and has smaller corrosiveness and pressure drop compared to water (Manda et al., 2020), which helps to reduce viscous and differential pressure resistance in the channel (Manda et al., 2021). Therefore, sCO2 may be more advantageous for drag reduction within microchannels. It should be noted that if sCO2 is used as the flow medium, due to its special physical properties, such as the special changes in density and viscosity in the supercritical state, the influence of gravity cannot be ignored during calculation (Manda et al., 2024). We should also claimed that the results of this study are more applicable to water.

However, the algorithm presented here can be extended to the study of other different fluid.

In summary, the conical microstructure experiences the least total resistance and has the best overall drag reduction.

4. CONCLUSIONS

In this study, 3D numerical simulations of conical microstructures of three different sizes, which were obtained through machining as described in (Wang et al., 2020b), were carried out. The impact of various size parameters on the drag-reduction effect of the conical microstructures was analyzed. Additionally, changes of the drag-reduction effect during the wear process of the conical microstructure were investigated. The surface drag-reduction effects of the conical microstructure to those of the worn round table microstructure, and V-shaped longitudinal and V-shaped transverse grooves were compared. Our findings can be summarized as follows:

(1) The drag-reduction effect observed in this study is consistent with the experimental results (Wang et al., 2020b), i.e., H-65 < H-95 < H-125. Increasing the width between adjacent conical microstructures (i.e., increasing the period length s) results in a greater average slip velocity and a better drag-reduction effect. While keeping the width of the conical microstructure constant, increasing the height leads to a decrease in the aspect ratio, resulting in a linear increase in drag-reduction rate and a better drag-reduction effect. Therefore, when preparing superhydrophobic surfaces with conical microstructures, increasing the width of the microstructure or appropriately reducing the aspect ratio of the conical microstructure is recommended.

(2) The tip of the conical microstructure is exposed to ultrahigh wall shear stress during the drag-reduction process, making it highly susceptible to wear. In the initial stages of wear, when the tip is rounded, there is an increase in the dimensionless pressure drop and drag-reduction rate, which is more conducive to drag-reduction. However, as the degree of wear increases, the increase in viscous resistance outweighs the reduction of differential pressure resistance, leading to a decrease in drag-reduction effectiveness.

(3) Conical microstructures demonstrate the best resistance reduction compared to round table microstructures, V-shaped longitudinal grooves, and V-shaped transverse grooves. While the longitudinal groove has the least differential pressure resistance and is second in drag reduction, the V-shaped longitudinal groove and the round table microstructure exhibit the highest viscous resistance and are third in drag reduction. The V-shaped transverse groove produces the greatest differential pressure resistance and is the least effective in reducing drag.

In this study, we investigated the overall drag-reduction effect of superhydrophobic surfaces. However, some flow details, such as the spurious currents phenomenon at the gas–liquid interface, need to be further investigated. Although we mentioned the possible reasons for spurious currents, some other factors needs to be considered. The 2D contact line (Noori et al., 2019) and 3D contact surfaces of gas–liquid will be studied in our future work.

ACKNOWLEDGMENTS

The authors acknowledge the School of Mathematics and Statistics, Henan University of Science and Technology, for allowing the use of their high-performance computing resources.

CONFLICT OF INTEREST

The authors have no conflicts to disclose.

AUTHORS CONTRIBUTION

Yuqian Xu: wrote the first version of the manuscript; contribute to the design and simulation; contributed to answering comments. **Chunlei Ruan**: supervision; review and editing; contributed to answering comments. **Zeyue Zhang**: review and editing; contributed to answering comments.

REFERENCES

Anderson, J. D. (1995). *Computational fluid dynamics: The basics with applications*. Beijing, China: Tsinghua University Press.

Blevins, R. D. (1984). Applied Fluid dynamics handbook. *New York, Van Nostrand Reinhold*.

Cassie, A. B. D. (1944). Wettability of porous surfaces, *Transactions of Faraday Society, 40*, 546-551. https://doi.org/10.1039/tf9444000546

Chen, Y. C., Huang, Z. S., & Yang. H. (2015). Cicada-wing-inspired self-cleaning antireflection coatings on polymer substrates. *Acs Applied Materials & Interfaces, 7*(45), 25495-25505. https://doi.org/10.1021/acsami.5b08743

Cui, Q. Z., Li, C. X., & Ye. X. M. (2017). Effect of structural parameters on the turbulent resistance characteristics of superhydrophobic microchannels, *Electric Power Science & Engineering*, *033*(007), 52-57. https://doi.org/10.3969/j.ISSN.1672-0792.2017.07.009

Davies, J., Maynes, D., Webb, B. W., & Woolford, B. (2006). Laminar flow in a microchannel with superhydrophobic walls exhibiting transverse ribs, *Physics of Fluids*, *18*(8), 87110. https://doi.org/10.1063/1.2336453

Hosseini, S., Savaloni, H., & Shahraki, M. (2019). Influence of surface morphology and nano-structure on hydrophobicity: A molecular dynamics approach, *Applied Surface Science*, *485*, 536-546. https://doi.org/10.1016/j.apsusc.2019.04.236

Kibar, A. (2022). A Liquid jet impinging onto rotating convex superhydrophobic and hydrophilic surfaces: Reflection or deflection?. *Journal of Applied Fluid*

Mechanics, 15(6), 1881-1888. https://doi.org/10.47176/jafm.15.06.1227

Li, C. X., Zhang, S., Xue, Q. X., & Ye, X. M. (2016). Simulation of drag reduction in superhydrophobic microchannels based on parabolic gas-liquid interfaces. *Physics of Fluids, 28*(10), 102004. https://doi.org/10.1063/1.4964757

Liu, Y. B., Gu, H. M, Jia, Y., Liu, J., Zhang, H., Wang, R. M., & Zhang, B. L. (2019). Design and preparation of biomimetic polydimethylsiloxane (Pdms) films with superhydrophobic, self-healing and drag reduction properties via replication of shark skin and si-atrp. *Chemical Engineering Journal, 356*, 318-328. https://doi.org/10.1016/j.cej.2018.09.022

Galvis, E., Yarusevych, S., & Culham, J. R. (2012). Incompressible laminar developing flow in microchannels. *Journal of Fluids Engineering*, *134*, 014503. https://doi.org/10.1115/1.4005736

Manda, U., & Mazumdar, S. (2023). Effects of cross-sectional shape on flow and heat transfer characteristics of the laminar flow of supercritical carbon dioxide inside horizontal microchannels. [Preprint]. https://ssrn.com/abstract=4635996

Manda, U., Mazumdar, S., & Peles, Y. (2024). Effects of buoyancy in a laminar flow of supercritical carbon dioxide in a horizontal microchannel at different gravities, *International Communications in Heat and Mass Transfer*, *150*, 107195. https://doi.org/10.1016/j.icheatmasstransfer.2023.107195

Manda, U., Parahovnik, A., Mazumdar, S., & Peles, Y. (2023). Heat transfer characteristics of turbulent flow of supercritical carbon dioxide (sCO2) in a short-heated microchannel. *International Journal of Thermal Sciences*, *192*, 108389. https://doi.org/10.1016/j.ijthermalsci.2023.108389

Manda, U., Parahovnik, A., & Peles, Y. (2020, July 21-23). *Theoretical investigation of boundary layer behavior and heat transfer of supercritical carbon dioxide (sCO2) in a microchannel*. 2020 19th IEEE Intersociety Conference on Thermal and Thermomechanical Phenomena in Electronic Systems (ITherm), Orlando, FL, USA. https://doi.org/10.1109/ITherm45881.2020.9190408

Manda, U., Parahovnik, A., & Peles, Y. (2022). Thermoacoustic waves and Piston Effect inside a microchannel with Carbon Dioxide near critical conditions. *Thermal Science and Engineering Progress*, *36*, 101528. https://doi.org/10.1016/j.tsep.2022.101528

Manda, U., Peles, Y., & Putnam, S. (2021, June 01-04). *Comparison of heat transfer characteristics of flow of supercritical carbon dioxide and water inside a square microchannel*. 2021 20th IEEE Intersociety Conference on Thermal and Thermomechanical Phenomena in Electronic Systems (iTherm), San Diego, CA, USA. https://doi.org/10.1109/ITherm51669.2021.9503192

Milionis, A., Loth, E., & Bayer, I. S. (2016). Recent advances in the mechanical durability of superhydrophobic materials. *Advances in Colloid & Interface Science, 229*, 57-79. https://doi.org/10.1016/j.cis.2015.12.007

Monfared, M., Alidoostan, M. A., & Saranjam, B. (2019). Experimental study on the friction drag reduction of superhydrophobic surfaces in closed channel flow. *Journal of Applied Fluid Mechanics, 12*(1), 69-76. https://doi.org/10.29252/jafm.75.253.28442

Noori, S. M. S., Rahni, M. T., & Taleghani, S. A. S. (2019) Multiple-relaxation time color-gradient lattice Boltzmann model for simulating contact angle in two-phase flow with high density ratio. *The European Physical Journal Plus*, *134*, 1-15. https://doi.org/10.1140/epjp/i2019-12759-x.

Ou, J., Perot, B., & Rothstein, J. P. (2004). Laminar drag reduction in microchannels using ultrahydrophobic surfaces, *Physics of Fluids, 16*(12), 4635-4643. https://doi.org/10.1063/1.1812011

Ou, J., & Rothstein, J. P. (2005). Direct velocity measurements of the flow past drag-reducing ultrahydrophobic surfaces. *Physics of Fluids, 17*(10), 103606. https://doi.org/10.1063/1.2109867

Rastegari, A., & Akhavan, R. (2019). On drag reduction scaling and sustainability bounds of superhydrophobic surfaces in high reynolds number turbulent flows, *Journal of Fluid Mechanics, 864*, 327-347. https://doi.org/10.1017/jfm.2018.1027

Song, B., Yuan, X., & Hu, H. (2012). Simulating flow field of superhydrophobic surface in laminar flow to reduce its drag, *Journal of Northwestern Polytechnical University, 30*(5), 712-717. https://doi.org/10.3969/j.issn.1000-2758.2012.05.015.

Tao, W. Q. (2001). *Numerical heat transfer(Second Edition)*. Xi'an, China: Xi'an Jiaotong University Press.

Tian, X., Verho, T., & Ras, R. (2016). Moving superhydrophobic surfaces toward real-world applications. *Science, 352*(6282), 142-143. https://doi.org/10.1126/science.aaf2073

Wang, D., Sun, Q., Hokkanen, M. J., Zhang, C., Lin, F. Y., Liu, Q., Zhu, S. P., Zhou, T., Chang, Q., He, B., Zhou, Q., Chen, L., Wang, Z., Ras, R. H. A., & Deng, X. (2020a). Design of robust superhydrophobic surfaces, *Nature, 582*(7810), 55-59. https://doi.org/10.1038/s41586-020-2331-8

Wang, L. Q., & Liu, X. M. (2007). Quadratic Tc-Bézier curves with shape parameter. *Computer Engineering and Design, 197*(05), 1096-1097.

Wang, Y., Gao, C., Zhao, W., Zheng, G., & Shen, C. (2020b). Large-Area fabrication and applications of patterned surface with anisotropic superhydrophobicity. *Applied Surface Science*, *529*, 147027. https://doi.org/10.1016/j.apsusc.2020.147027

Watanabe, S., Mamori, H., & Fukagata, K. (2017). Drag-reducing performance of obliquely aligned superhydrophobic surface in turbulent channel flow, *Fluid Dynamics Research, 49*(2), 025501. https://doi.org/10.1088/1873-7005/49/2/025501

Xu, Y., Zhang, C., & Wang, Z. X. (2021). Sinulation analysis on drag reduction performance of characteristic parameters of v-groove on local approximate plane. *Aeronautical Manufacturing Technology, 64*(15), 86-99. https://doi.org/10.16080/j.issn1671-833x.2021.15.086

Yang, X. H., Fu, T. T., Jiang, S. K., Zhu, C. Y., & Ma, Y. G. (2018). Progress in pressure drop of fluid in microchannels, *The Chinese Journal of Process Engineering, 18*(4), 680-688. https://doi.org/10.12034/j.issn.1009-606X.217406

Zhang, J., Zhang, Y., Yong, J., Hou, X., & Chen, F. (2022). Femtosecond laser direct weaving bioinspired superhydrophobic/hydrophilic micro-pattern for fog harvesting. *Optics Laser Technology, 146*, 107593. https://doi.org/10.1016/j.optlastec.2021.107593

Zhang, W., Xiang, T., Liu, F., Zhang, M., Gan, W., Zhai, X., Di, X., Wang, Y., Liu, G., & Wang, C. (2017). Facile design and fabrication of superwetting surfaces with excellent wear-resistance. *Acs Applied Materials Interfaces, 18*(9), 15776-15784. https://doi.org/10.1021/acsami.7b02158